CONF-890393--2

UCRL- 100198
PREPRINT



# FAR FIELD PROJECTION

Marvin J. Barth
Richard W. Ziolkowski

This paper is being prepared for submittal
to the Fifth Annual Review of Progress
in Applied Computational Electromagnetics
Monterey, California
March 21-23, 1989

January 4, 1989

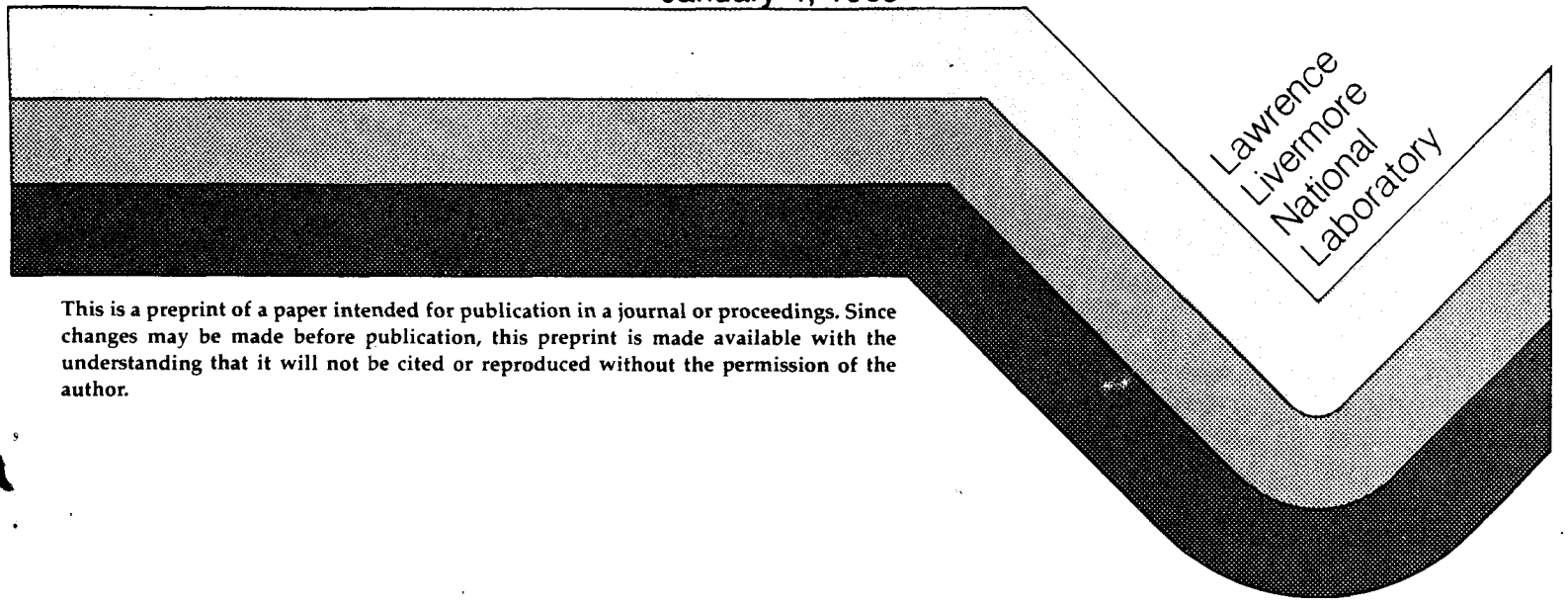

---

## DISCLAIMER

# FAR FIELD PROJECTION

UCRL--100198

DE89 010243

Dr. Marvin J. Barth and Dr. Richard W. Ziolkowski
Lawrence Livervore National Laboratory
P. O. Box 5504, L-156
Livermore. CA 94550

**ABSTRACT**

The FAR computer code, which post processes the results of a Finite Difference Time Domain (FDTD) code to produce far-field quantities from near-field values, is described. The integral equation and differential equation approaches are two methods of calculating the radiation and scattering effects of systems. Each method has practical limitations when used in general application codes. For instance, integral equation approaches such as the method of moments usually consider only perfectly conducting wires and patches in the frequency domain and the differential equation approaches such as FDTD, while applicable to multi-media and the time domain, are constrained to finite volumes determined by the specific computer memories. The FAR code allows the near-field details in the time domain modeled by FDTD codes to be extended to the far-field. This combined FDTD-FAR code set greaty extends the class of numerical electromagnetic modeling problems that can be treated with discrete differential equation methods.

The FAR code uses the equivalence principle. Specifically, the code utilizes the tangential electric and magnetic fields at a specified surface of the FDTD computational volume and calculates the resulting far-fields from the equivalent magnetic and electric sources. In this process the sources of errors are sampling density, the length of the excitation pulse, the total time history record length, the time step size, and the size of the FDTD volume. The FDTD-FAR approach will be illustrated with a pulse driven array of dipole elements. The far-field time histories and the resulting frequency domain antenna patterns will be presented. The sizes of the various errors in this approach will be discussed in detail. The efficacy of this approach will be contrasted with conventional methods.

## I. INTRODUCTION

The finite difference time domain (FDTD) codes have several advantages including the ability to model very complex and elaborate systems, multi-media, and multiple frequencies (through Fourier inversion). The disadvantage of FDTD codes is that the problems they model are generally limited by the size of the available computer memory; hence, only the near-field may be modeled. The Lawrence Livermore National Laboratory (LLNL) developed code, FAR, will be described in this paper. It is a postprocessing code that uses the near-field results of discrete codes to determine the corresponding far-field in either the time or frequency domain.

The output of a FDTD code is the time domain $\vec{E}$ and $\vec{H}$ fields at the different grid points throughout the computational volume. With these $\vec{E}$ and $\vec{H}$ values we use the equivalence principle to define equivalent electrical and magnetic currents on a specified surface in this computational space. The projection of these dipole currents to the far-field is achieved with standard frequency and time domain dipole field formulas.

We assume zero sources outside the computational volume and use Maxwell's boundary conditions with a null field internal to the volume to determine the surface currents which would produce the same external field. For this condition, the magnetic($\vec{J}$) and electric($\vec{M}$) currents are:

$$\vec{J}_s = \hat{n} \times \vec{H} \qquad (1)$$

$$\vec{M}_s = \vec{E} \times \hat{n} \tag{2}$$

It should be noted that we do not have the exact surfaces currents from the grid values given in the FDTD codes but only point values of these currents. This approximation will cause some error which we will discuss later.

Since exterior to this equivalent source surface the problem is linear (interior to the computational volume, the finite element methods allow some types of non-linearity), we assign the far-field of an equivalent infinitesimal dipole to each point of that surface and sum over all these surface points.

The field of an infinitesimal electric dipole may be determined by calculating the fields in the Fourier domain and transforming into the time domain. The equations for the dipole $\vec{\epsilon}$ field is [1]:

$$\vec{\epsilon} = \frac{-\mu}{4\pi r}\epsilon^{-\jmath kr}(j\omega)\vec{P} \tag{3}$$

$$\vec{P} = p(\omega)(\hat{u}_x p^x + \hat{u}_y p^y + \hat{u}_z p^z) \tag{4}$$

where $\{p^x, p^y, p^z\}$ are components of a unit vector pointing in the direction of the point source and $p(\omega)$ is a scalar corresponding to dipole strength. For an array of $N_J$ electric sources, equation (4) can be summed as:

$$\vec{E}_J(\omega, \vec{R}) = \frac{-\mu}{4\pi}\sum_{i=1}^{N_J}\frac{1}{r_i}e^{-\jmath kr_i}(j\omega)p_i(\omega)\{\hat{u}_x p_i^x + \hat{u}_y p_i^y + \hat{u}_z p_i^z\} \tag{5}$$

$$r_i = |\vec{R} - \vec{r}_i'| \tag{6}$$

$$\vec{R} = \hat{u}_x X + \hat{u}_y Y + \hat{u}_z Z \tag{7}$$

$$\vec{r}_i' = \hat{u}_x x_i' + \hat{u}_y y_i' + \hat{u}_z z' \tag{8}$$

Capital letters will always designate total fields and the observer distance whereas primes will indicate the source coordinates. Since we are calculating the far-field, we follow the usual conventions and remove the inverse distance term $R = |\vec{R}|$ from the summation sign and treat the phase term as [1]:

$$r_i = R - \psi_i \tag{9}$$

$$\psi_i = x_i' \sin\theta\cos\phi + y_i' \sin\theta\sin\phi + z_i' \cos\theta \tag{10}$$

Transforming into spherical coordinates will result in:

$$E_{J\theta}(\omega, \vec{R}) = -K\mu(\cos\theta\cos\phi S_{Jx} + \cos\theta\sin\phi S_{Jy} - \sin\theta S_{Jz}) \tag{11}$$

$$E_{J\phi}(\omega, \vec{R}) = K\mu(\sin\phi S_{Jx} - \cos\phi S_{Jy}) \tag{12}$$

$$H_{J\theta} = \frac{-E_{J\phi}}{\eta} \tag{13}$$

$$H_{J\phi} = \frac{E_{J\theta}}{\eta} \tag{14}$$

$$K = \frac{e^{-jkR}}{4\pi R} \tag{15}$$

$$S_{Jx} = j\omega \sum_{i=1}^{N_J} e^{jk\psi_i} p_i(\omega) p_i^x \tag{16}$$

$$S_{Jy} = j\omega \sum_{i=1}^{N_J} e^{jk\psi_i} p_i(\omega) p_i^y \tag{17}$$

$$S_{Jz} = j\omega \sum_{i=1}^{N_J} e^{jk\psi_i} p_i(\omega) p_i^z \tag{18}$$

In equations (13) and (14) we have designated the medium impedance as $\eta = (\mu/\epsilon)^{1/2}$. The radiation field pattern is then a plot of $|RE_\theta|$ or $|RE_\phi|$. As R approaches infinity, the phase relation used in (14) is exact.

The time domain fields may be obtained from the inverse Fourier transform, i.e.,

$$E(t) = \frac{1}{2\pi} \int_{-\infty}^{\infty} E(\omega) e^{j\omega t} d\omega \tag{19}$$

To transform these into the time domain we will use the time shifting and time differentiation properties:

$$\text{for} \qquad f(t) \leftrightarrow F(\omega) \iff f(t - t_0) \leftrightarrow F(\omega) e^{-j\omega t_0} \tag{20}$$

$$\text{and for} \qquad f(t) \leftrightarrow F(\omega) \iff \frac{df}{dt} \leftrightarrow (j\omega) F(\omega) \tag{21}$$

The time domain fields from the electric sources can be written as:

$$E_{J\theta}(t, \vec{R}) = -K' \mu (\cos\theta \cos\phi S'_{Jx} + \cos\theta \sin\phi S'_{Jy} - \sin\theta S'_{Jz}) \tag{22}$$

$$E_{J\phi}(t, \vec{R}) = K' \mu (\sin\phi S'_{Jx} - \cos\phi S'_{Jy}) \tag{23}$$

$$K' = \frac{1}{4\pi R} \tag{24}$$

$$S'_{Jx} = \sum_{i=1}^{N_J} \frac{d}{dt'_i} p_i(t'_i) p_i^x \tag{25}$$

$$S'_{Jy} = \sum_{i=1}^{N_J} \frac{d}{dt'_i} p_i(t'_i) p_i^y \tag{26}$$

$$S'_{Jz} = \sum_{i=1}^{N_J} \frac{d}{dt'_i} p_i(t'_i) p_i^z \tag{27}$$

In these field expressions the retarded time is:

$$t'_i = t - \frac{R}{c} + \frac{\psi}{c} \tag{28}$$

The fields for magnetic sources are found by duality.

## II. VALIDATION

We selected a problem involving two infinitesimal dipoles radiating in free space for our validations. The geometry is shown in Figure 1. The driving function and its Fourier transform are shown in Figures 2 and 3. We generally considered results at 1.0 GHz near the peak of the frequency spectrum.

We used four combinations of codes in our tests: TSAR-FAR, XNEAR-FAR, JOB, and NEC. TSAR is a LLNL developed FDTD code. XNEAR is a code which calculates the exact output of two infinitesimal dipoles and outputs the results in the same format as TSAR. JOB is a derivative of XNEAR which calculates the exact field at points on the specified equivalent current simulation surface. NEC is the LLNL developed Numerical Electromagnetics Code. The XNEAR-FAR comparison with NEC yields the errors due solely to FAR. The TSAR-FAR comparison with NEC yields the overall error. In computing the errors we made frequency plots of $\vec{E}_\theta$ in two planes: the horizonal plane ($\theta = 90; -90 \leq \phi \leq 90$) and the vertical plane ($\phi = 0; 0 \leq \theta \leq 180$). The error was then the maximum difference between the NEC and FAR plots. Figures 4 and 5 show a comparison between the TSAR-FAR and NEC predicted patterns at 1.0GHz in the horizonal and the vertical planes respectively when the dipoles are driven with the pulse shown in Fig. 2 and both a "10 cells and 20 cells per wavelength" discretization is used in TSARS.

Here we report on four types of errors we have uncovered and studied. We term these errors: discrete Fourier transform (DFT) errors, averaging errors, grid size errors, and frequency errors.

(1) *Discrete Fourier Transform Errors*

The FAR code has a subroutine which takes the DFT of the time domain TSAR (or XNEAR) output and then projects the DFT to the far-field. There are three types of errors inherit with the numerical DFT subroutines: aliasing, leakage, and picket-fence [2],[3].

Aliasing is caused by the sampling rate. It occurs when the high frequency components of the time signal impersonate a low frequency component. Since the time record is finite, the frequency transform will be infinite and there is no absolute cure for the error. The best that can be done is to design the excitation pulse as one which has most of the energy near the frequency of interest and to use a sampling frequency which is much higher.

Both leakage and the picket-fence errors are caused by using a time signal of finite duration. This is equivalent to multiplying (in the time domain) an infinite duration time signal by a window of amplitude one with the same duration as that of the time signal. In the frequency domain this is equivalent to a convolution of the time signal's Fourier transform and the "$\sin x/x$" Fourier transform of the window. The result is that each discrete frequency impulse of the time signal is replaced with the "$\sin x/x$" function and all "$\sin x/x$" functions summed.

Leakage refers to the error caused by the summation of the trailing ends of the "$\sin x/x$" functions. If there is a DC component to the time signal this error is exacerbated because the discontinuity of the signal at the record end will produce many more frequency points with each point convolved with the "$\sin x/x$" functions. The method of mitigation for

leakage errors is to multiply the time history by a window other than the rectangular window or to use a transit pulse (one which begins and ends at zero).

The picket-fence error is caused when the frequency of interest is not an exact multiple of the sampling frequency. (Here the series of "$\sin x/x$" functions act as filters in the frequency domain giving a picket-fence effect.) There are two cures which mitigate this effect. The first is to take the DFT at multiples of the sampling frequency and then to perform complex interpolation. The other is to "zero-pack" the time signal (i.e., add a large number of zero points to the time signal which creates a much longer time signal). The effect of zero-packing is to spread out the frequency components.

To mitigate the effects of aliasing, we use a pulse which has most of its energy at and below 1.0GHz and has continuous derivatives. One such pulse is termed the Z-pulse[4]. The equations describing this pulse for a period from zero to one are:

$$f(x) = 32x^3 - 48x^4 \qquad \text{for} \qquad 0 \le x \le 0.5 \tag{29}$$

$$f(x) = 32(1-x)^3 - 48(1-x)^4 \qquad \text{for} \qquad 0 \le x \le 0.5 \tag{30}$$

Although this pulse is good with reference to aliasing, it still has a poor characteristic with reference to leakage. In the near-field, the dipole is a sum of three terms, each proportional to the original excitation pulse, its derivative, and its integral. As is seen the integral term of the Z-pulse would have a DC term and thus a leakage problem. In order to mitigate the leakage effect, we have found that either a Half Hamming window or a Half Blackman window will give good results. The equations for these windows are:

$$W_H(x) = 0.54 - 0.56\cos\left(\frac{2\pi(x-1)}{M-1}\right) \tag{31}$$

$$W_B(x) = 0.42 - 0.5\cos\left(\frac{2\pi(x-1)}{M-1}\right) + 0.08\cos\left(\frac{4\pi(x-1)}{M-1}\right) \tag{32}$$

where M = the pulse length and the range is $M/2 \le x \le M$.

A better pulse (i.e., a transit pulse), with all the good characteristics of the Z-pulse is its derivative termed the DZ-pulse. It is described by the equations:

$$f(x) = 96x^2 - 192x^3 \qquad \text{for} \qquad 0 \le x \le 0.5 \tag{33}$$

$$f(x) = -96(1-x)^2 + 192(1-x)^3 \qquad \text{for} \qquad 0 \le x \le 0.5 \tag{34}$$

Figures 2 and 3 show this pulse for a time of 5.0e-11 sec. and a period of 120.0e-11 sec. It can be seen that most of the energy is below 2.0e9 Hz. and it has continuous derivatives.

We have found that a good choice of the excitation pulse will produce minimum aliasing and leakage errors. To account for the picket-fence error we have found that zero-packing to an order 12 yields results as good as any higher packing. (By zero-packing to an order 12 we mean to increase the time record by $2^{12}$ zeros. It should be pointed out that the time records are not actually increased by this amount, but with the proper choice of sampling frequency in the DFT subroutine, the DFT appears to add this order of zeros.)

(2) *Averaging Errors*

Another source of error is due to the staggered grid used in the FDTD calculations. The magnetic and electric fields are not recorded at the same spatial point in the FDTD

codes. We have chosen the measurement surface such that the the electric field calculation points exactly lie on it. Since the offsets for the magnetic fields are at half points on the grid cell, two sets of the magnetic field are computed, and then averaged to determine the magnetic field values on the measurement surface. This averaging process introduces an additional error.

To investigate the magnitude of the error introduced by this averaging two codes were used: XNEAR which calculates the magnetic fields at the half points (the same points as TSAR) and JOB. The other variables were set as follows:

(1) Frequency, f = 1.0GHz
(2) Grid size, Dx = $\lambda/10$
(3) Time sampling size, Dt = 5.0 e-11 sec.
(4) Time record length, NTOT = 201
(5) Zero packing order, ISTEP = 3
(6) Pulse = Z-Pulse
(7) Window = Half Hamming

Figure 6 shows the averaged (XNEAR) and exact (JOB) time records of the magnetic field $H_y$ at the center of the front face of the measurement surface. The maximum percent error between these two curves is 3.53%. There are 2548 measurement points for the magnetic field over the six surfaces of this problem. When the horizonal pattern plot is compared with NEC the resulting errors are:

XNEAR error = 2.5793 %
JOB error = 0.6447 %

Thus, magnetic field averaging introduces an additional 1.8547% error in the far-field electric field patterns.

(3) *Grid Size Errors*

The grid size ($Dx$) is set in the FDTD code. In addition to wavelength sampling criterions, practical considerations such as the size of computer memory and near-field detail dictate the grid size. With decreasing grid size, more surface values of $\vec{E}$ and $\vec{H}$ are output and, from an information view, the more accurate the results of FAR will be. The objective of this part of our study was to quantify this effect.

We used the JOB code to investigate this error. This precluded FDTD or averaging errors and allowed us to concentrate on the grid size errors. In addition this choice premitted cost efficient code runs with grid sizes from $\lambda/6$ to $\lambda/20$ to be made.

When executing a FDTD code, the Courant condition sets a limit on the time sampling size ($Dt$). Therefore, as we varied Dx we correspondly varied $Dt$ by the relation $Dt = Dx/c$ (where $c$ is the velocity of light). Table 1 indicates the error associated with these variations. It is seen that major improvements occur with decreasing the grid size until $\lambda/10$ at which the rate of improvement decreases.

| Dx | Dt | Final Error |
|---|---|---|
| $\lambda/6$ | 8.333333e-11 | 1.750 |
| $\lambda/8$ | 6.250000e-11 | 0.949 |
| $\lambda/10$ | 5.000000e-11 | 0.594 |
| $\lambda/12$ | 4.166667e-11 | 0.402 |
| $\lambda/16$ | 3.125000e-11 | 0.247 |
| $\lambda/20$ | 2.500000e-11 | 0.159 |

**TABLE 1.**

Error Variation with respect to $Dx$

We also made code runs with variations of $Dt$ while holding $Dx$ constant to test the error effects of $Dt$ variations. Throughout the $Dx$ range of $\lambda/6$ to $\lambda/20$ we found negligible error.

(4) *Frequency Errors*

The last type of error we report on is the effect of varying the frequency while holding the geometry shown in Fig. 1 fixed. Figures 7 and 8 show horizonal plane plots at frequencies of 0.5GHz and 1.5GHz of TSAR-FAR and NEC. We made code runs at every 0.1GHz over this range at grid sizes of $\lambda/10$ and $\lambda/20$. In these code runs we have found maximum errors from 1.0% up to 20.0% when comparing the electric field pattern plots with NEC. (The average errors are on the order of up to 5.0%.) Figure 9 shows these pattern plot maximum errors as a function of frequency for XNEAR (which produces the exact dipole fields at the measurement surfaces) and TSAR-FAR (with a grid size of $\lambda/20$). With reference to the pattern plots shown in Figures 4, 7, and 8 it can be seen that these maximum errors occur at the nulls and peaks of the pattern near the endfire directions.

At this point we do not understand completely the causes of these errors. We do believe that a major factor of the error is associated with the sampling of the surface currents. That is, at lower frequencies (and longer wavelengths) our sampling density over the surface is greater, i.e., there are more samples per square wavelength. In contrast, at higher frequencies the sampling density decreases. Figure 10 shows a comparison of the sampling density (normalized to the error at 1.0GHz) and the XNEAR-FAR error over the range of frequencies. As can be seen the general trend of the curves support our contention. The fine structure remains to be investigated.

## III. CONCLUSIONS

A limitation of FDTD codes has been the inability to model radiation and scattering effects of systems at distances far from their sources. At LLNL we have developed the code FAR which, using the equivalence principle, projects the computational surface time-domain $\vec{E}$ and $\vec{H}$ fields from a FDTD code to the far-field. The code output may be in either the frequency or time domain. This paper has described that code and its validation.

The major errors associated with this near-to-far-field procedure were identified and discussed. As noted above, we have tried to quantify these errors thoroughly. We grouped the errors as DFT, averaging, grid size, and frequency errors.

The aliasing, leakage, and picked-fence errors are always present whenever a DFT is used; thus, they are absent whenever time domain results are desired. The aliasing error may be mitigated with the proper choice of input pulse. We have found that the Z and DZ-pulses reduce aliasing to a negligible effect. Because the Z-pulse, when used as a dipole excitation, produces a DC term, windows must be used to mitigate the leakage effect. We have found the Half Hamming and Half Blackman windows to be adequate in these cases. The picked-fence error is negligible when "zero-packing" to the 12-th order is used. The averaging error is caused when the $\vec{H}$ field is averaged to make it coincident with the electric field values on the measurement surfaces. This error will account for approximately 2% of the total error. The grid size is set by the FDTD code parameters. The range of error is from slightly less than 0.16% to 2.0%. Although smaller grid sizes are desirable, we have found that a $\lambda/10$ choice is a good one. Here, $\lambda$ corresponds to the frequency of interest. This choice is also appropiate when considering the FDTD parameters. Although we have not completed our investigation of frequency errors, we have found the error proportional to the surface sampling density (measurement points / square wavelengths). Choosing a grid size of $\lambda/10$ will produce good results (approximately 5% errors). The error is reduced at lower frequencies. It appears that when higher frequency results are required, the problem should be run with a grid spacing account for this fact.

## ACKNOWLEDGMENTS

This work was performed by the Lawrence Livermore National Laboratory under the auspices of the U. S. Department of Energy under contract No. W-7405-ENG-48.

## REFERENCES

[1] Roger F. Harrington, *Time-Harmonic Electromagnetic Fields*, (New York:McGraw-Hill,1961).

[2] G. D. Bergland, "A Guided Tour Of The Fast Fourier Transform", *IEEE Spectrum*, p. 41-52, July 1969.

[3] Fredric J. Harris, "On The Use Of Windows For Harmonic Analysis With The Discrete Fourier Transform", *Proc. IEEE*, Vol. 66, No. 1, p. 172-204, January 1978.

[4] Richard W. Ziolkowski, Niel K. Madsen, and Robert C. Carpenter, "Three-Dimensional Computer Modeling Of Electromagnetic Fields: A Global Lookback Lattice Truncation Scheme", *J. Comp. Phy.*, Vol. 50, No. 3, p. 360-408, June 1983.

## FIGURE CAPTIONS

Figure 1. Geometry for the two pulsed dipole problem ( Frequency = 1.0GHz, $\lambda$ = 0.2997925m).

Figure 2. The input excitation pulse that drives each dipole. (Time Domain)

Figure 3. The Fourier transform of the input dipole excitation pulse. (Frequency Domain)

Figure 4. The horizontal pattern plot for $\theta = 90$, and $-90 \leq \phi \leq 90$ predicted at 1.0GHz by *NEC* (—-), *TSAR-FAR* $\lambda/20$ (- - -), and *TSAR-FAR* $\lambda/10$ $(\cdots)$.

Figure 5. The vertical pattern plot for $\phi = 0$, and $0 \leq \theta \leq 180$ predicted at 1.0GHz

by *NEC* (—-), *TSAR-FAR* $\lambda/20$ (- - -), and *TSAR-FAR* $\lambda/10$ $(\cdots)$.

Figure 6. The time record of the magnetic field for *JOB(exact)* (—-) and *XNEAR(average)* (- - -) at a measurement point on the front face.

Figure 7. The horizonal pattern plot for $\theta = 90$, and $-90 \leq \phi \leq 90$ predicted at 0.5GHz by *NEC* (—-), *TSAR-FAR* $\lambda/20$ (- - -), and *TSAR-FAR* $\lambda/10$ $(\cdots)$.

Figure 8. The horizonal pattern plot for $\theta = 90$, and $-90 \leq \phi \leq 90$ predicted at 1.5GHz by *NEC* (—-), *TSAR-FAR* $\lambda/20$ (- - -). and *TSAR-FAR* $\lambda/10$ $(\cdots)$.

Figure 9. The maximum pattern plot error for *XNEAR* (—-) and *TSAR-FAR* $\lambda/20$ (- - -) as a function of frequency.

Figure 10. A comparison of the *XNEAR* (—-) maximum pattern plot error and the *NORMALIZED SAMPLING DENSITY* (- - -).

Top View

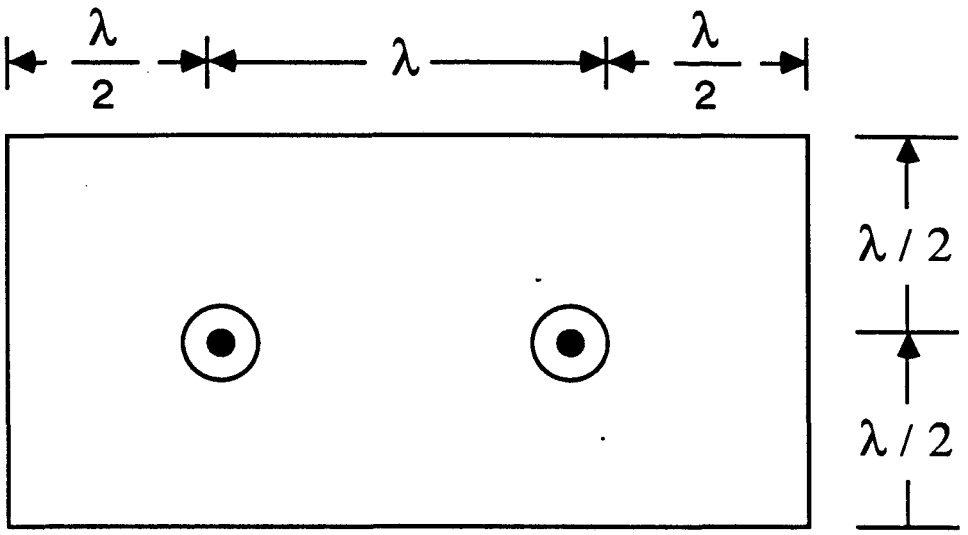


Side View

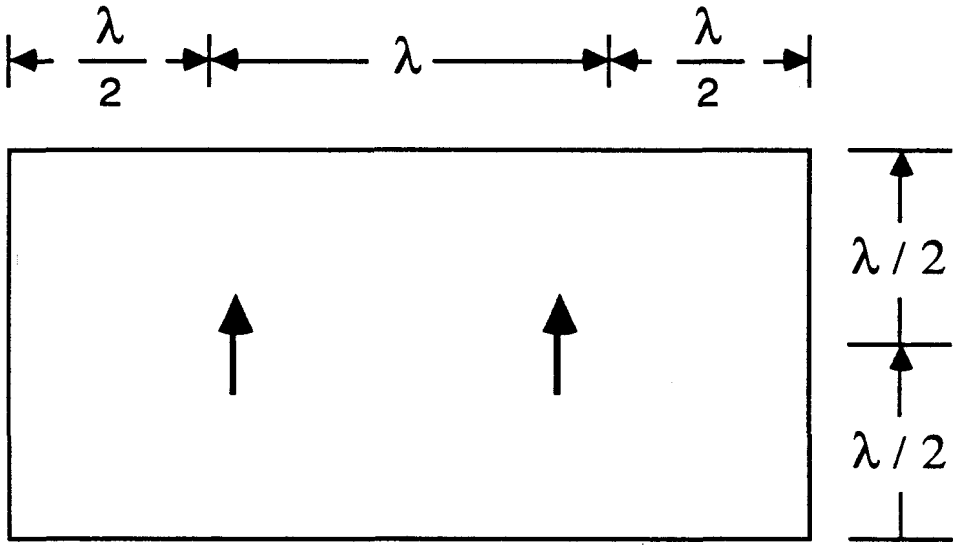


End View

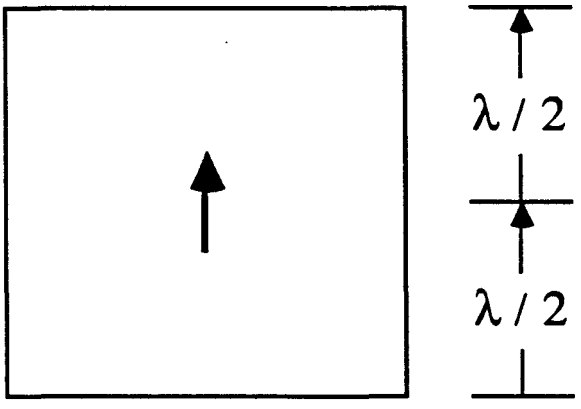


Figure 1.

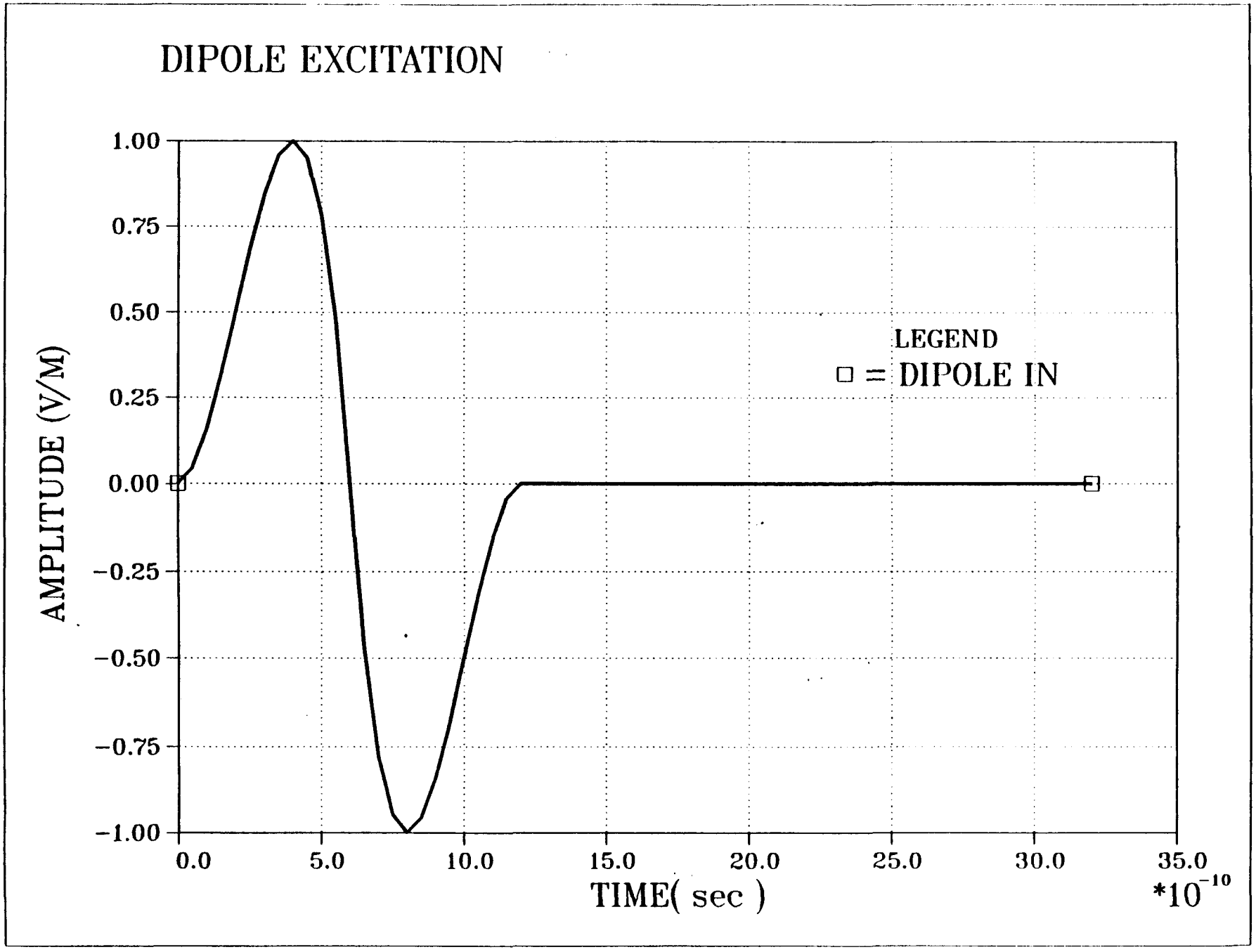
DIPOLE EXCITATION
AMPLITUDE (V/M)
1.00
0.75
0.50
0.25
0.00
-0.25
-0.50
-0.75
-1.00
0.0
5.0
10.0
15.0
20.0
25.0
30.0
35.0
TIME( sec )
*10^-10
LEGEND
□ = DIPOLE IN

Figure 2.

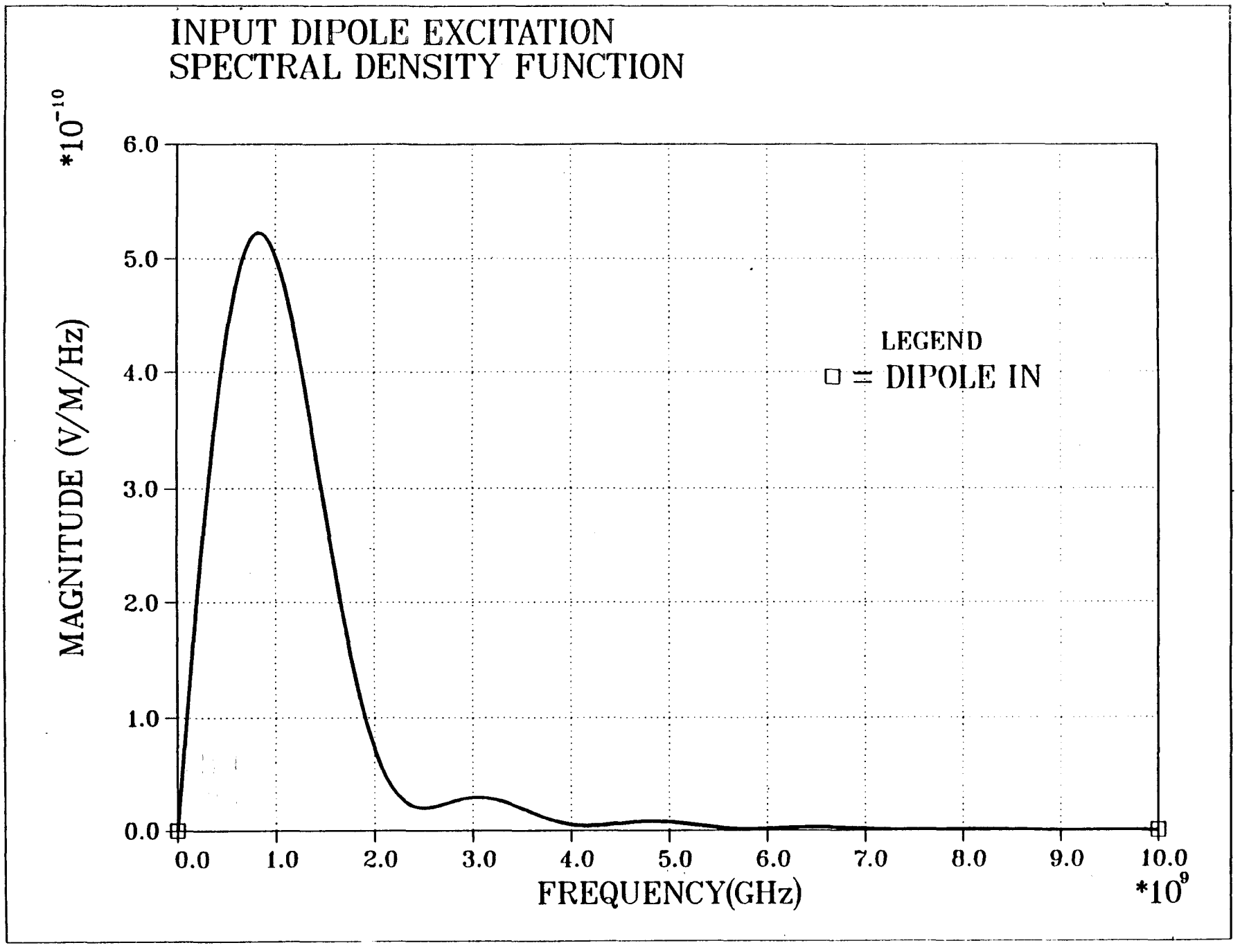
INPUT DIPOLE EXCITATION
SPECTRAL DENSITY FUNCTION
*10^-10
MAGNITUDE (V/M/Hz)
6.0
5.0
4.0
3.0
2.0
1.0
0.0
LEGEND
DIPOLE IN
0.0
1.0
2.0
3.0
4.0
5.0
6.0
7.0
8.0
9.0
10.0
FREQUENCY(GHz)
*10^9

Figure 3.

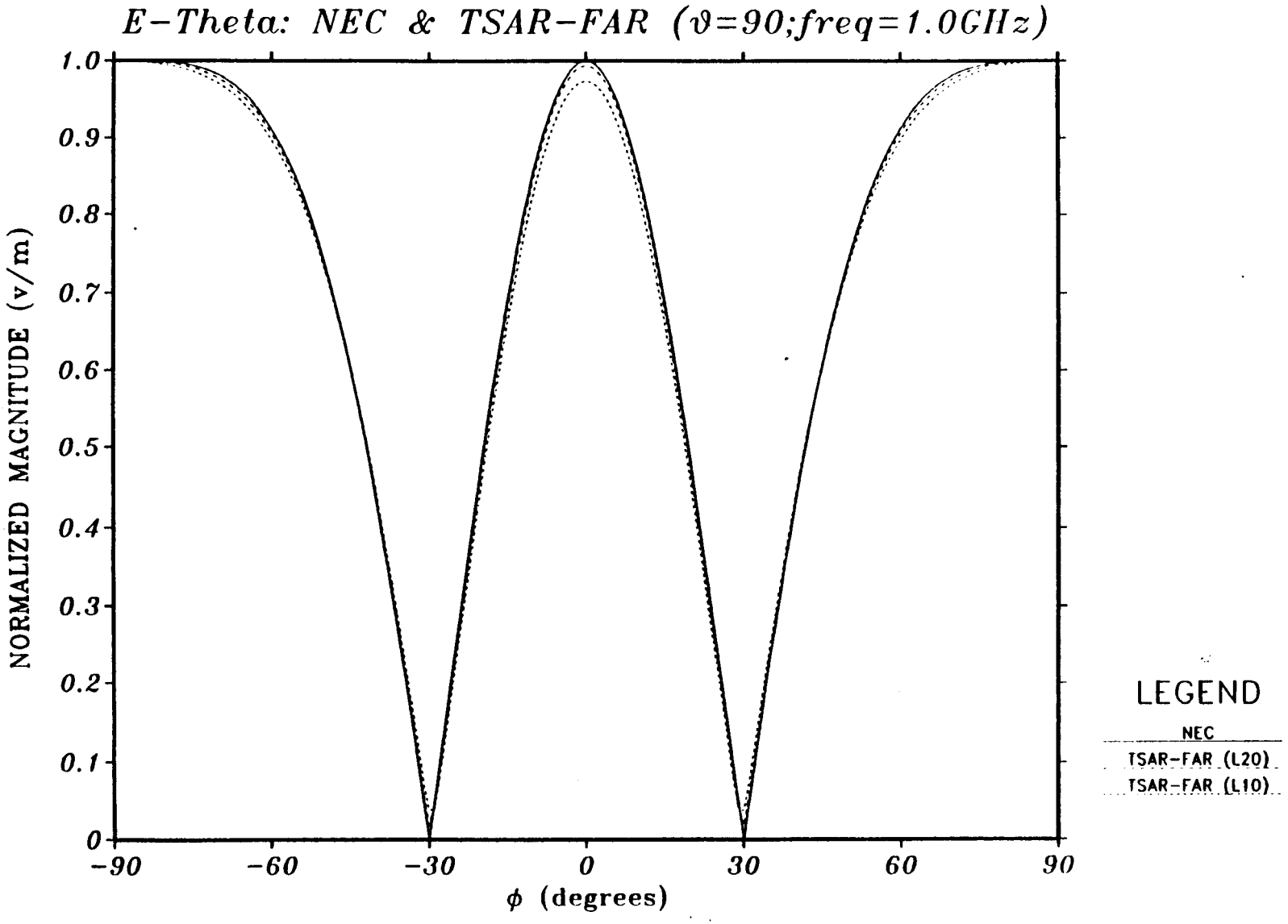
E-Theta: NEC & TSAR-FAR (ϑ=90;freq=1.0GHz)
NORMALIZED MAGNITUDE (v/m)
1.0
0.9
0.8
0.7
0.6
0.5
0.4
0.3
0.2
0.1
0
-90
-60
-30
0
30
60
90
ϕ (degrees)
LEGEND
NEC
TSAR-FAR (L20)
TSAR-FAR (L10)

Figure 4.

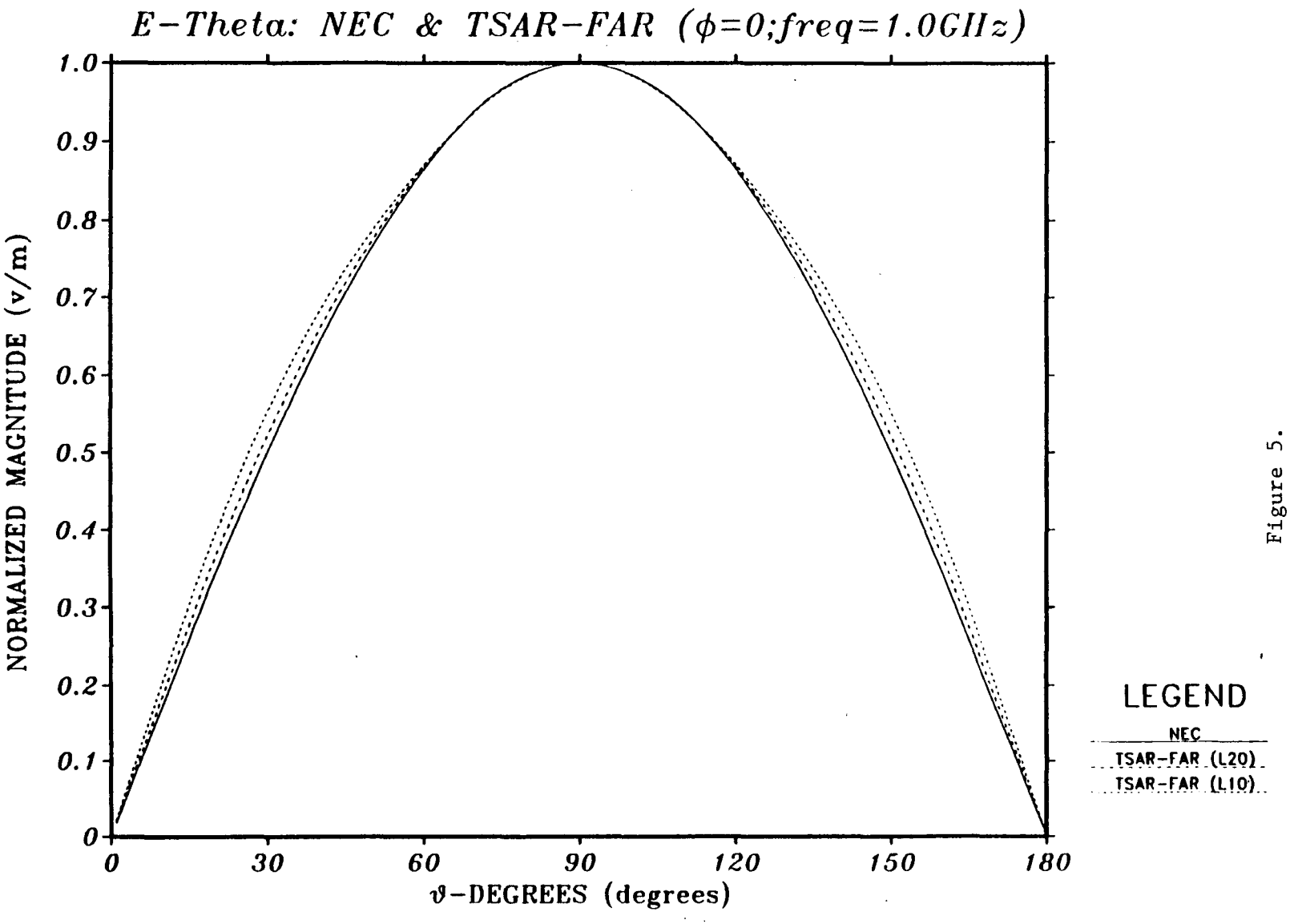
E-Theta: NEC & TSAR-FAR (ϕ=0;freq=1.0GHz)
NORMALIZED MAGNITUDE (v/m)
1.0
0.9
0.8
0.7
0.6
0.5
0.4
0.3
0.2
0.1
0
0
30
60
90
120
150
180
ϑ-DEGREES (degrees)
LEGEND
NEC
TSAR-FAR (L20)
TSAR-FAR (L10)

Figure 5.

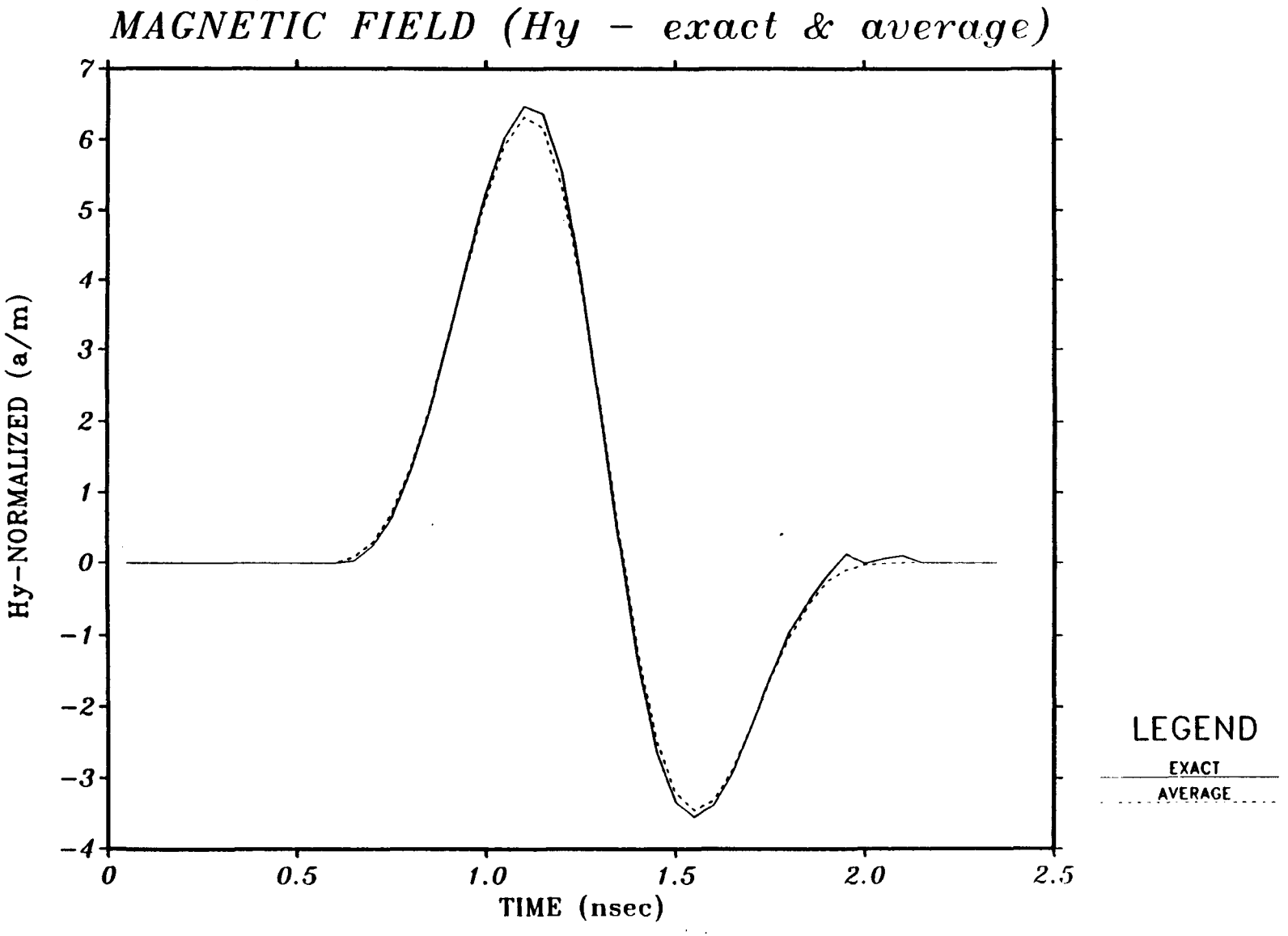
MAGNETIC FIELD (Hy - exact & average)
Hy-NORMALIZED (a/m)
7
6
5
4
3
2
1
0
-1
-2
-3
-4
0
0.5
1.0
1.5
2.0
2.5
TIME (nsec)
LEGEND
EXACT
AVERAGE

Figure 6.

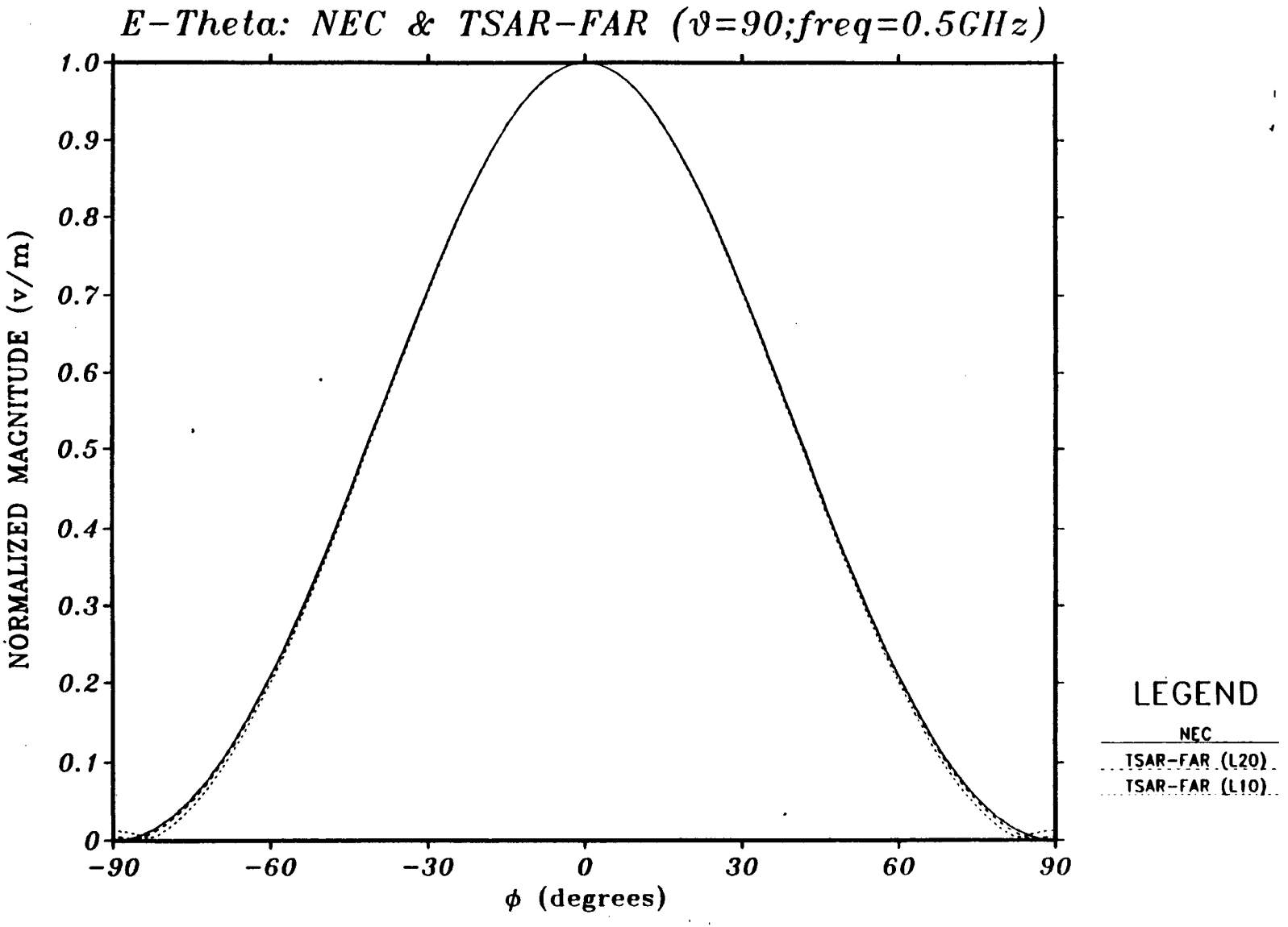
E-Theta: NEC & TSAR-FAR (ϑ=90;freq=0.5GHz)
NORMALIZED MAGNITUDE (v/m)
1.0
0.9
0.8
0.7
0.6
0.5
0.4
0.3
0.2
0.1
0
-90
-60
-30
0
30
60
90
ϕ (degrees)
LEGEND
NEC
TSAR-FAR (L20)
TSAR-FAR (L10)

Figure 7.

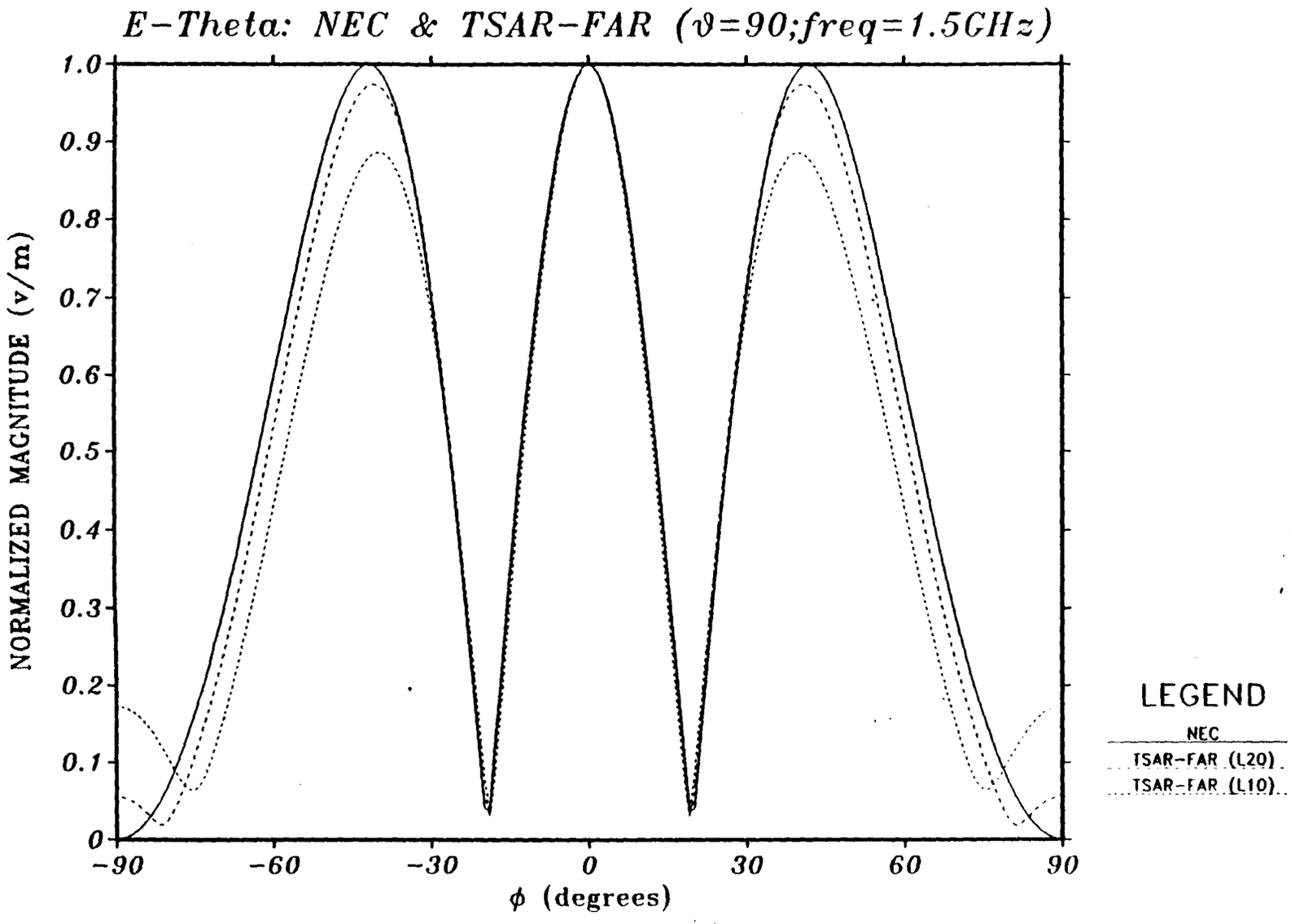
E-Theta: NEC & TSAR-FAR (ϑ=90;freq=1.5GHz)
NORMALIZED MAGNITUDE (v/m)
1.0
0.9
0.8
0.7
0.6
0.5
0.4
0.3
0.2
0.1
0
-90
-60
-30
0
30
60
90
ϕ (degrees)
LEGEND
NEC
TSAR-FAR (L20)
TSAR-FAR (L10)

Figure 8.

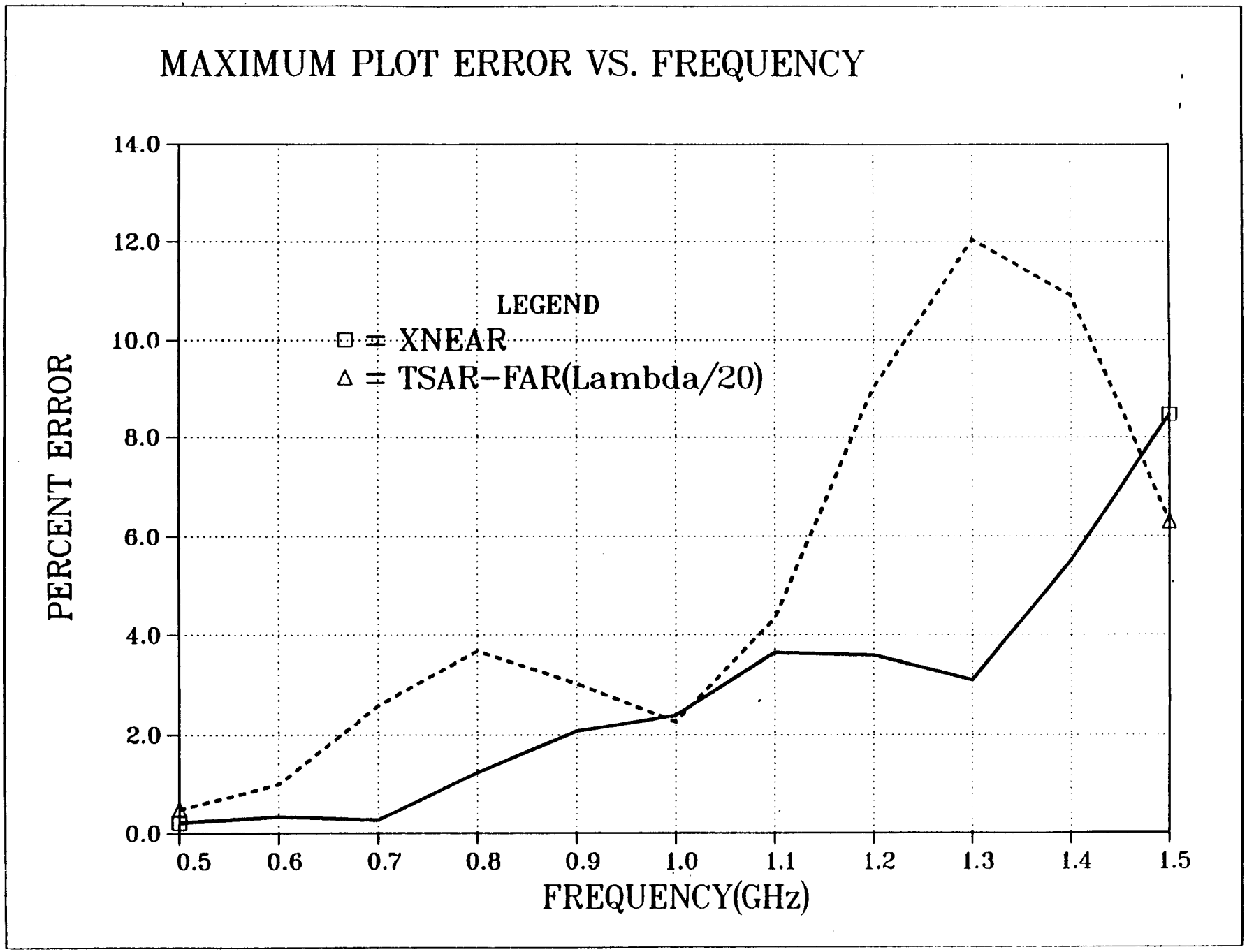
MAXIMUM PLOT ERROR VS. FREQUENCY
PERCENT ERROR
14.0
12.0
10.0
8.0
6.0
4.0
2.0
0.0
LEGEND
□ = XNEAR
△ = TSAR-FAR(Lambda/20)
0.5
0.6
0.7
0.8
0.9
1.0
1.1
1.2
1.3
1.4
1.5
FREQUENCY(GHz)

Figure 9.

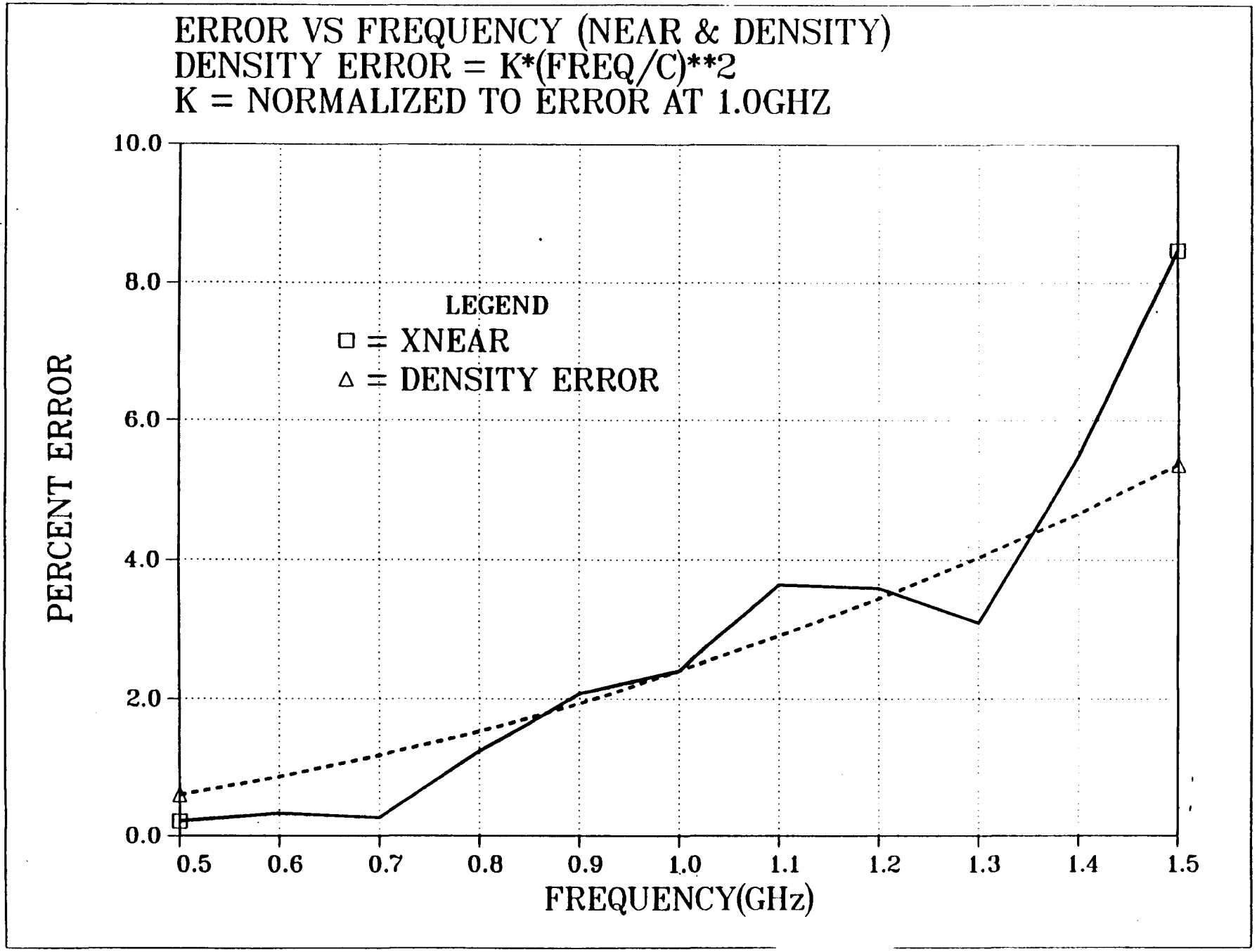
ERROR VS FREQUENCY (NEAR & DENSITY)
DENSITY ERROR = K*(FREQ/C)**2
K = NORMALIZED TO ERROR AT 1.0GHZ
PERCENT ERROR
10.0
8.0
6.0
4.0
2.0
0.0
LEGEND
□ = XNEAR
△ = DENSITY ERROR
0.5
0.6
0.7
0.8
0.9
1.0
1.1
1.2
1.3
1.4
1.5
FREQUENCY(GHz)

Figure 10.